

## Spectroscopic and Electronic Structure Studies of Protocatechuate 3,4-Dioxygenase: Nature of Tyrosinate–Fe(III) Bonds and Their Contribution to Reactivity

Mindy I. Davis,<sup>†</sup> Allen M. Orville,<sup>‡,§</sup> Frank Neese,<sup>†,||</sup> Jeffrey M. Zaleski,<sup>†,⊥</sup>  
John D. Lipscomb,<sup>\*,‡</sup> and Edward I. Solomon<sup>\*,†</sup>

*Contribution from the Department of Chemistry, Stanford University, Stanford, California 94305-5080, and the Department of Biochemistry, Molecular Biology and Biophysics and the Center for Metals in Biocatalysis, University of Minnesota, Minneapolis, Minnesota 55455*

Received August 10, 2001

**Abstract:** The geometric and electronic structure of the high-spin ferric active site of protocatechuate 3,4-dioxygenase (3,4-PCD) has been examined by absorption (Abs), circular dichroism (CD), magnetic CD (MCD), and variable-temperature–variable-field (VT-VH) MCD spectroscopies. Density functional (DFT) and INDO/S-CI molecular orbital calculations provide complementary insight into the electronic structure of 3,4-PCD and allow an experimentally calibrated bonding scheme to be developed. Abs, CD, and MCD indicate that there are at least seven transitions below 35 000 cm<sup>-1</sup> which arise from tyrosinate ligand-to-metal-charge transfer (LMCT) transitions. VT-VH MCD spectroscopy gives the polarizations of these LMCT bands in the principal axis system of the *D*-tensor, which is oriented relative to the molecular structure from the INDO/S-CI calculations. Three transitions are associated with the equatorial tyrosinate and four with the axial tyrosinate. This large number of transitions per tyrosinate is due to the  $\pi$  and importantly the  $\sigma$  overlap of the two tyrosinate valence orbitals with the metal *d* orbitals and is governed by the Fe–O–C angle and the Fe–O–C–C dihedral angles. The previously reported crystal structure indicates that the Fe–O–C angles are 133° and 148° for the equatorial and axial tyrosinate, respectively. Each tyrosinate has transitions at different energies with different intensities, which correlate with differences in geometry that reflect pseudo- $\sigma$  bonding to the Fe(III) and relate to reactivity. These factors reflect the metal–ligand bond strength and indicate that the axial tyrosinate–Fe(III) bond is weaker than the equatorial tyrosinate–Fe(III) bond. Furthermore, it is found that the differences in geometry, and hence electronic structure, are imposed by the protein. The consequences to catalysis are significant because the axial tyrosinate has been shown to dissociate upon substrate binding and the equatorial tyrosinate in the enzyme–substrate complex is thought to influence asymmetric binding of the chelated substrate moiety via a strong trans influence which activates the substrate for reaction with O<sub>2</sub>.

### Introduction

Oxygen-activating enzymes with mononuclear non-heme iron active sites perform a variety of important biological functions.<sup>1–5</sup> The bacterial catechol dioxygenases are important in the aerobic

degradation of nearly all naturally occurring and xenobiotic aromatic compounds.<sup>3,6,7</sup> These widely distributed enzymes catalyze the cleavage of molecular oxygen with concomitant insertion of both oxygen atoms into the aromatic ring of the substrate, resulting in ring cleavage. The catechol dioxygenases can be divided into two broad subclasses based on the site of ring opening, the intra- and extradiol cleaving enzymes. The intradiol dioxygenases contain an Fe(III) center, which facilitates the cleavage of the aromatic ring between the hydroxylated carbon atoms. In contrast, the extradiol dioxygenases utilize an Fe(II) (and rarely Mn(II))<sup>8</sup> center to regiospecifically cleave the ring on either the distal or proximal side of the vicinal hydroxyl groups of the substrate.<sup>3</sup> In addition to the correlation of metal

\* Corresponding authors.

<sup>†</sup> Stanford University.

<sup>‡</sup> University of Minnesota.

<sup>§</sup> Current Address: School of Chemistry and Biochemistry, Georgia Institute of Technology, Atlanta, GA 30332.

<sup>||</sup> Current Address: Max Planck Institut für Strahlenchemie, Mülheim an der Ruhr, Germany D-45470.

<sup>⊥</sup> Current Address: Department of Chemistry, Indiana University, Bloomington, IN 47405.

(1) Feig, A. L.; Lippard, S. J. *Chem. Rev.* **1994**, *94*, 759–805.

(2) Hegg, E. L.; Que, L., Jr. *Eur. J. Biochem.* **1997**, *250*, 625–629.

(3) Lipscomb, J. D.; Orville, A. M. In *Degradation of Environmental Pollutants by Microorganisms and Their Metalloenzymes*; Sigel, H., Sigel, A., Eds.; Marcel Dekker: New York, 1992; Vol. 28, pp 243–298.

(4) Que, L., Jr.; Ho, R. Y. N. *Chem. Rev.* **1996**, *96*, 2607–2624.

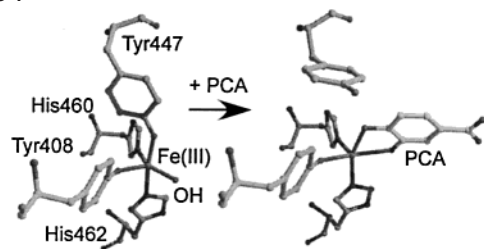
(5) Solomon, E. I.; Brunold, T.; Davis, M. I.; Kemsley, J. N.; Lee, S.-K.; Lehnert, N.; Neese, F.; Skulan, A. J.; Yang, Y.-S.; Zhou, J. *Chem. Rev.* **2000**, *100*, 235–349.

(6) Dagley, S. In *The Bacteria*; Sokatch, J. R., Ornston, L. N., Eds.; Academic Press: Orlando, 1986; Vol. 10, Chapter 10, pp 527–555.

(7) Levin, M. A.; Gealt, M. A. In *Biotreatment of Industrial and Hazardous Waste*; Levin, M. A., Gealt, M. A., Eds.; McGraw-Hill: New York, 1993; pp 5–7.

(8) Boldt, Y. R.; Sadowsky, M. J.; Ellis, L. B. M.; Que, L., Jr.; Wackett, L. P. *J. Bacteriol.* **1995**, *177*, 1225–1232.

Scheme 1



redox state with ring cleavage site, the proposed mechanisms of oxygen activation/reactivity differ for the two enzyme classes.<sup>3–5</sup> Because of the persistence of the ferric redox state throughout the reaction cycle, the intradiol dioxygenases are proposed to coordinate and then activate the aromatic substrate for direct attack by dioxygen. In contrast, the extradiol dioxygenases are proposed to bind the aromatic substrate at the ferrous center, which consequently increases the affinity of the Fe(II) center for coordination and activation of O<sub>2</sub>.

Protocatechuate 3,4-dioxygenase (3,4-PCD, EC 1.13.11.3), an extensively studied intradiol cleaving catecholic dioxygenase, catalyzes the cleavage of protocatechuate (PCA; 3,4-dihydroxybenzoate) to  $\beta$ -carboxy-*cis,cis*-muconate with the incorporation of both oxygen atoms from molecular oxygen.<sup>9</sup> Because this is a key reaction in many aromatic compounds,<sup>3</sup> the enzyme has been isolated from or identified in over a dozen bacterial species.<sup>3</sup> The 3,4-PCDs isolated from *Brevibacterium fuscum*, *Pseudomonas putida*, and *Acinetobacter calcoaceticus* ADP1 are perhaps the best characterized. Indeed there are currently 19 X-ray crystallographic structures available for 3,4-PCD as isolated from *P. putida* and *A. calcoaceticus* ADP1 and in numerous ligand complexes with substrates, substrate analogues, inhibitors, and oxygen analogues.<sup>10–15</sup> In addition, crystal structures of catechol 1,2-dioxygenase (1,2-CTD), another member of the intradiol dioxygenase family, are also available as isolated from *A. calcoaceticus* and in several ligand complexes.<sup>15</sup> In every structurally defined example, the geometry of the high-spin ferric center as isolated is distorted trigonal bipyramidal with histidine and tyrosinate as the axial ligands and histidine, tyrosinate, and a water-based (or rarely, sulfate) ligand as the equatorial ligands (see Scheme 1 for the 3,4-PCD active site from *P. putida*). The water-based ligand has been proposed to be a hydroxide by X-ray absorption spectroscopy (XAS) of 3,4-PCD from *B. fuscum* and *P. putida*, and thus charge neutrality of the active site can be inferred.<sup>16,17</sup> Key X-ray crystallographic bond lengths and angles and the bond lengths obtained from the extended X-ray absorption fine structure analysis (EXAFS) from 3,4-PCD are given in Table 1.

**Table 1.** Metal–Ligand Bond Lengths of 3,4-PCD from X-ray Crystallography and EXAFS, and Bond Angles from X-ray Crystallography

	EXAFS <sup>a</sup>	X-ray crystallogr <sup>b</sup>
Fe–Tyr408	1.88 Å	1.81 Å
Fe–His460	2.10 Å	2.33 Å
Fe–His462	2.10 Å	2.26 Å
Fe–Tyr447	1.88 Å	1.90 Å
Fe–OH	1.88 Å	1.91 Å
Fe–O–C <sub>tyr447</sub>		148°
Fe–O–C–C <sub>tyr447</sub>		24°
Fe–O–C <sub>tyr408</sub>		133°
Fe–O–C–C <sub>tyr408</sub>		68°

<sup>a</sup> Bond lengths for the enzyme from *B. fuscum* as determined by EXAFS in ref 17. <sup>b</sup> The average bond lengths and angles calculated from the six independent protomers in the asymmetric unit of *P. putida* 3,4-PCD as determined by X-ray crystallography (from PDB code 2PCD, ref 14).

A characteristic of all intradiol dioxygenases is their burgundy-red color that arises from tyrosinate ligand-to-metal charge transfer transitions (LMCT). Spectroscopic and crystallographic analyses have demonstrated that tyrosinate–Fe(III) ligation is also present in the transferrin family of iron carriers<sup>18–21</sup> and the binuclear purple acid phosphatases.<sup>22–26</sup> The absorption spectrum of each of these metalloproteins is similar and is dominated by a moderately intense absorption maximum in the 400–600 nm region that is attributed to tyrosinate LMCT transitions. The position of the LMCT transitions in both tyrosinate–iron enzymes and model complexes has been shown to vary in energy and intensity depending on the ligand environment.<sup>27–31</sup> The difference in geometric and electronic structure can have important functional ramifications.

The dynamic iron coordination sphere of 3,4-PCD has been demonstrated by spectroscopic, crystallographic, and kinetic studies.<sup>10–13,16,32,33</sup> These results have shown that, upon substrate binding, the axial tyrosinate and equatorial hydroxide are displaced by substrates, which bind in a chelated doubly deprotonated form. Additionally, the coordination of the anaerobic substrate complex is asymmetric with the longer bond trans to Tyr408 (the equatorial tyrosinate),<sup>13,16,32,33</sup> and the active site geometry shifts to square pyramidal with an open coordination position trans to His460 (Scheme 1). Crystallographic and kinetic studies of the Y447H mutant isoform of 3,4-PCD

- (9) Fujisawa, H.; Hayaishi, O. *J. Biol. Chem.* **1968**, *243*, 267–281.
- (10) Elgren, T. E.; Orville, A. M.; Kelly, K. A.; Lipscomb, J. D.; Ohlendorf, D. H.; Que, L., Jr. *Biochemistry* **1997**, *36*, 11504–11513.
- (11) Frazee, R. W.; Orville, A. M.; Dolbear, K. B.; Yu, H.; Ohlendorf, D. H.; Lipscomb, J. D. *Biochemistry* **1998**, *37*, 2131–2144.
- (12) Orville, A. M.; Lipscomb, J. D.; Ohlendorf, D. H. *Biochemistry* **1997**, *36*, 10052–10066.
- (13) Orville, A. M.; Elango, N.; Lipscomb, J. D.; Ohlendorf, D. H. *Biochemistry* **1997**, *36*, 10039–10051.
- (14) Ohlendorf, D. H.; Orville, A. M.; Lipscomb, J. D. *J. Mol. Biol.* **1994**, *244*, 586–608.
- (15) Vetting, M. W.; D'Argenio, D. A.; Ornston, L. N.; Ohlendorf, D. H. *Biochemistry* **2000**, *39*, 7943–7955.
- (16) True, A. E.; Orville, A. M.; Pearce, L. L.; Lipscomb, J. D.; Que, L., Jr. *Biochemistry* **1990**, *29*, 10847–10854.
- (17) Davis, M. I.; Wasinger, E. C.; Westre, T. E.; Zaleski, J. M.; Orville, A. M.; Lipscomb, J. D.; Hedman, B.; Hodgson, K. O.; Solomon, E. I. *Inorg. Chem.* **1999**, *38*, 3676–3683.

- (18) Gaber, B. P.; Miskowski, V.; Spiro, T. G. *J. Am. Chem. Soc.* **1974**, *96*, 6868–6873.
- (19) Carey, P. R.; Young, N. M. *Can. J. Biochem.* **1974**, *52*, 273–280.
- (20) MacGillivray, R. T. A.; Moore, S. A.; Chen, J.; Anderson, B. F.; Baker, H.; Luo, Y.; Bewley, M.; Smith, C. A.; Murphy, M. E. P.; Wang, Y.; Mason, A. B.; Woodworth, R. C.; Brayer, G. D.; Baker, E. N. *Biochemistry* **1998**, *37*, 7919–7928.
- (21) Day, C. L.; Anderson, B. F.; Tweedie, J. W.; Baker, E. N. *J. Mol. Biol.* **1993**, *232*, 1084–1100.
- (22) Klabunde, T.; Krebs, B. *Struct. Bonding* **1997**, *89*, 177–198.
- (23) Klabunde, T.; Strater, N.; Fröhlich, R.; Witzel, H.; Krebs, B. *J. Mol. Biol.* **1996**, *259*, 737–748.
- (24) McRee, D. E.; Bruns, C. M.; Williams, P. A.; Mietzner, T. A.; Nunn, R. PDB code 1D9Y, to be published.
- (25) Uppenberg, J.; Lindqvist, F.; Svensson, C.; Ek-Rylander, B.; Anderson, G. *J. Mol. Biol.* **1999**, *290*, 201–211.
- (26) Bruns, C. M.; Nowalk, A. J.; Arvai, A. S.; McTigue, M. A.; Vaughan, K. G.; Mietzner, T. A.; McRee, D. E. *Nat. Struct. Biol.* **1997**, *4*, 919–924.
- (27) Que, L., Jr. *Coord. Chem. Rev.* **1983**, *50*, 73–108.
- (28) Casella, L.; Gullotti, M.; Pintar, A.; Messori, L.; Rockenbauer, A.; Györ, M. *Inorg. Chem.* **1987**, *26*, 1031–1038.
- (29) Pyrz, J. W.; Roe, A. L.; Stern, L. J.; Que, L., Jr. *J. Am. Chem. Soc.* **1985**, *107*, 614–620.
- (30) He, Q.-Y.; Mason, A. B.; Woodworth, R. C.; Tam, B. M.; MacGillivray, R. T. A.; Grady, J. K.; Chasteen, N. D. *Biochemistry* **1997**, *36*, 14853–14860.
- (31) Bull, C.; Ballou, D. P. *J. Biol. Chem.* **1981**, *256*, 12673–12680.
- (32) Orville, A. M.; Lipscomb, J. D. *J. Biol. Chem.* **1989**, *264*, 8791–8801.
- (33) Whittaker, J. W.; Lipscomb, J. D. *J. Biol. Chem.* **1984**, *259*, 4487–4495.

indicated that the observed 600-fold decrease in  $k_{\text{cat}}$  of the mutant isoform relative to wild type (WT) was due to much slower rates of substrate binding and product release.<sup>11</sup> Structural analysis suggests that the lack of iron coordination by the H447 residue is partially responsible for the altered characteristics of the mutant isoform. However, despite these differences, the substrate-bound forms of the mutant isoform and wild-type enzymes, which have indistinguishable optical spectra, each react with oxygen with similar and very rapid rates. Therefore, the axial tyrosinate which is more solvent exposed appears to influence catalysis in a dynamic manner by dissociating and facilitating deprotonation of the second substrate hydroxyl group. In contrast, the equatorial tyrosinate, which has no significant solvent-exposed surface and is static in all crystal structures analyzed to date, appears to exert a strong trans influence that increases bond length of the ligand–metal bond trans to it.<sup>12,14,34,35</sup> One of the proposed mechanisms<sup>3,4,36,37</sup> for substrate activation and specific intradiol reactivity involves this elongation of the substrate Fe–O bond trans to Tyr408 which may facilitate facile ketonization of the C3–O bond of substrate molecules during oxygen attack. The distal oxygen atom of the ensuing peroxy-substrate intermediate may bind to the vacant coordination site opposite His460, thereby facilitating O–O bond cleavage and intradiol ring cleavage. Therefore, the trans influence from the equatorial tyrosinate and the dissociation of the axial tyrosinate are both mechanistically important, but the underlying geometric and electronic structural features that yield such different behavior by the two tyrosinate ligands remains to be explained.

In this investigation, circular dichroism (CD), low-temperature magnetic CD (MCD), variable-temperature–variable-field (VTVH) MCD, and UV–visible absorption (Abs) coupled with density functional theory (DFT) and INDO/S-CI molecular orbital (MO) calculations have been used to determine the electronic structure of the active site of 3,4-PCD and to correlate it with the geometric structure. The nature of the resting structure and its spectroscopic features were examined, as well as the nature of and differences between the two tyrosinate–Fe(III) bonds and their contributions to reactivity. Additionally, the role of the second coordination sphere on the tyrosinate–Fe(III) geometric and electronic structure was explored. CD, MCD, VTVH MCD, and Abs allow the resolution of seven electronic transitions. By using recently developed methodology, the VTVH MCD data can be used to obtain the polarizations of each band relative to the principal axis of the zero-field-splitting (ZFS) tensor (also called  $D$ -tensor).<sup>38–40</sup> This provides polarization information on a randomly oriented sample, where previously such data were possible only from single-crystal polarized absorption spectroscopy. Orbital descriptions and the associated transitions were determined using DFT and INDO/S-CI calculations. Using the recently developed ZFS methodology, in addition to calculating  $D$  (including sign) and  $E/D$ , the  $D$ -tensor can be mapped onto the active site structure.<sup>41,42</sup> This relates

the band polarizations obtained from the VTVH MCD data to the active site structure and allows assignment of the electronic transitions. Applied to a protein for the first time, these methods provide detailed geometric and electronic structural information that enables the detailed assignment of the spectroscopic data which provides a description of the tyrosinate–Fe(III) bond, the effect of the Fe–O–C and Fe–O–C–C angles<sup>43</sup> on the two tyrosinate–Fe(III) bonds, and an understanding of the role of the tyrosinate–Fe(III) bonds in reactivity.

## Experimental Section

**Sample Preparation.** All commercial reagents were of the highest grade available and used without further purification. Protocatechuate 3,4-dioxygenase from *Brevibacterium fuscum* was purified as previously reported, stored at  $-80^{\circ}\text{C}$ , and thawed immediately prior to use.<sup>44,45</sup> The Abs and CD spectra and other selected comparisons of 3,4-PCD isolated from *P. putida* and *B. fuscum* were identical in both the oxidized and the reduced forms.<sup>17,34</sup> Therefore, it is reasonable to make comparisons between the spectroscopic studies on *B. fuscum* 3,4-PCD (which yield the most well-resolved features) and the crystal structures of *P. putida* 3,4-PCD. The 50 mM MOPS buffer (3-[*N*-morpholino]-propanesulfonic acid; Sigma) was adjusted to pH 7.0 with NaOH (Sigma). For the MCD experiments, 50% (v/v) glycerol, degassed under vacuum by freeze/pump/thaw/heat procedures, was added as a glassing agent. CD and Abs spectra were taken with and without glycerol present to ensure that the site was unaffected by the glassing agent. The iron concentration of the samples was 0.33 mM for the UV–visible CD/Abs/MCD and 2.0 mM for the near-IR CD/MCD. MOPS buffer prepared in  $\text{D}_2\text{O}$  (99.9 atom % D; Aldrich) and adjusted to a pD of 6.6 with NaOD (Sigma), and glycerol- $\text{d}_3$  (98 atom % D; Cambridge Isotopes Laboratories) was used to eliminate the hydroxide overtones that dominate the IR absorption spectrum above 1600 nm.

**Abs Spectroscopy.** UV/visible Abs spectra (200–820 nm) were recorded at room temperature on an HP8452A diode array spectrometer in a 0.5 cm path length quartz cuvette. Low-temperature absorption spectra (5 K) were obtained on a Cary 17 spectrometer equipped with a Janis Research Super Vari-temp helium cryogenic Dewar mounted in the light path.

**CD and MCD Spectroscopy.** The near-IR data were collected on a Jasco J-200D (600–2140 nm) spectropolarimeter with a liquid  $\text{N}_2$ -cooled InSb detector. The J-200D is equipped with an Oxford Instruments SM4000-7 tesla (T) superconducting magnet/cryostat capable of fields up to 7 T and temperatures down to 1.5 K. The UV/visible data were collected on a Jasco J-500C (200–1060 nm) with an extended S-20 and S-1 photomultiplier tube (Hamamatsu). The J-500C is equipped with an Oxford Instruments SM4-7 T superconducting magnet/cryostat capable of fields up to 7 T and temperatures down to 1.5 K.

CD samples were prepared in a 1 cm path length cuvette and were kept at  $4^{\circ}\text{C}$  at all times with a circulating cooling bath attached to the sample holder. Buffer and cell baselines were subtracted from the raw protein CD spectra. Low-temperature (1.6–50.2 K) MCD spectra were obtained in a copper MCD sample cell with two Infrasil quartz disks sandwiching a 3 mm thick neoprene O-ring spacer into which the sample was injected. MCD samples were quickly frozen in liquid  $\text{N}_2$  immediately after preparation. The depolarization of the frozen MCD sample, checked by measuring the CD spectrum of a nickel (+)-tartrate solution placed before and after the sample, was less than 5%.<sup>46</sup>

- (34) Orville, A. M.; Lipscomb, J. D. *Biochemistry* **1997**, *36*, 14044–14055.  
(35) Siu, D. C.-T.; Orville, A. M.; Lipscomb, J. D.; Ohlendorf, D. H.; Que, L., Jr. *Biochemistry* **1992**, *31*, 10443–10448.  
(36) Bugg, T. D. H.; Lin, G. *Chem. Commun.* **2001**, 941–952.  
(37) Funabiki, T.; Yamazaki, T. *J. Mol. Catal. A* **1999**, *120*, 37–47.  
(38) Neese, F.; Solomon, E. I. *Inorg. Chem.* **1999**, *38*, 1847–1865.  
(39) Oganessian, V. S.; Thomson, A. J. *J. Chem. Phys.* **2000**, *113*, 5003–5017.  
(40) Oganessian, V. S.; George, S. J.; Cheesman, M. R.; Thomson, A. J. *J. Chem. Phys.* **1999**, *110*, 762–777.  
(41) Neese, F.; Solomon, E. I. *J. Am. Chem. Soc.* **1998**, *120*, 12829–12848.

- (42) Neese, F.; Solomon, E. I. *Inorg. Chem.* **1998**, *37*, 6568–6582.  
(43) The dihedral angle discussed here is defined as the angle of the plane of the aromatic ring and the plane defined by the Fe–O–C atoms.  
(44) Whittaker, J. W.; Lipscomb, J. D.; Kent, T. A.; Münck, E. *J. Biol. Chem.* **1984**, *259*, 4466–4475.  
(45) Whittaker, J. W.; Orville, A. M.; Lipscomb, J. D. *Methods Enzymol.* **1990**, *188*, 82–88.  
(46) Browett, W. R.; Fucaloro, A. F.; Morgan, T. V.; Stephens, P. J. *J. Am. Chem. Soc.* **1983**, *105*, 1868–1872.



The MCD spectra were corrected for the natural CD and zero-field baseline effects caused by strain in the glasses by subtracting the 0 T scan from each of the other field scans at a given temperature. The Abs, CD, and MCD spectra were iteratively fit to Gaussian band shapes by using a modified Levenberg–Marquardt constrained least-squares fitting routine. For VTVH MCD spectroscopy, a calibrated carbon-glass or Cernox resistor (Lakeshore Cryotronics, calibrated 1.5–300 K) inserted in the sample cell was used to accurately measure the temperature of the sample. VTVH MCD data were analyzed using the theory and associated fitting program developed in ref 38.

**Electronic Structure Calculations. A. Active Site Geometry.** The active site geometric structure was obtained from the averaged crystallographic coordinates of *P. putida* 3,4-PCD (as depicted in Scheme 1) with the ligand–metal bond lengths modified by EXAFS results (Table 1).<sup>14,16,17,47</sup> Hydrogen atoms were placed at standard bond lengths and angles. The hydrogen atom on the hydroxide ligand was placed in the minimum energy conformation from a Hartree–Fock level minimization routine using INDO/S-CI. Additionally, each tyrosine ligand was symmetrized. The following model was used for the calculations: a hydroxide, imidazoles to model the two histidines, and phenolates to model the two tyrosinates. All other internal coordinates were left unchanged. Cartesian coordinates of the models (with the iron at the origin) used in the calculations are included as Supporting Information (Table S1).

**B. DFT Calculations.** The Amsterdam density functional (ADF 2.0.1) program developed by Baerends et al. was used.<sup>48,49</sup> The calculations were run on either an IBM 3BT-RS/6000 or SGI workstation. The local density approximation (LDA) of Vosko and co-workers was used,<sup>50</sup> together with the gradient corrections of Becke for the exchange<sup>51</sup> and of Perdew for the correlation (BP86).<sup>52</sup> The calculations were spin-polarized with an uncontracted triple- $\zeta$  basis set (ADF basis set IV) with a single polarization function used for all atoms. Core orbitals were frozen through 1s (C, N, O) and 3p (Fe). Calculations were accepted as converged when the maximum element in the error matrix, which is defined as the commutator of the Fock matrix and the density matrix, was less than  $10^{-5}$ . Graphical output of the computational results was generated with the Cerius<sup>2</sup> software program (Molecular Simulations, Inc.).

Geometry optimization at the BP86 level of theory with LANL2DZ basis set was carried out using the Gaussian 98 program suite.<sup>53</sup> The initial geometry was as described above, and the set of optimized internal coordinates was generated by the default redundant coordinate method. The optimization converged to a stationary point which has three imaginary frequencies ( $\nu \sim 400, 300$ , and  $100 \text{ cm}^{-1}$ ). These modes correspond to changes in intramolecular hydrogen bonds (C–H $\cdots$ O bond formation) among the equatorial tyrosinate and the hydroxide.<sup>54</sup>

This optimized geometry was used for a single point ADF calculation to provide Mulliken and Hirschfeld charges for comparison to the unoptimized active site calculation.

**C. Semiempirical Calculations.** Semiempirical INDO/S-CI calculations were carried out with the program Orca developed by F.N. The INDO/S model of Zerner and co-workers,<sup>55–58</sup> the valence shell ionization potentials and Slater–Condon parameters listed by Bacon and Zerner,<sup>58</sup> and the standard interaction factors  $f_{p\sigma p\sigma} = 1.266$  and  $f_{p\pi p\pi} = 0.585$  were used. Restricted open-shell Hartree–Fock (ROHF) self-consistent-field (SCF) calculations were tightly converged to the  $^6A_1$  ground state which served as a reference for configuration interaction (CI) calculations. The CI matrix was formed using a Rumer diagram algorithm. Stable results were obtained for the sextet spin states by including all single excitations into the singly occupied MOs (SOMOs), and from the SOMOs into all virtual orbitals, together with the double excitations from the highest 16 doubly occupied MOs (DOMOs) into the SOMOs. This scheme leads to 1671 configuration-state functions (CSFs) for this site with no symmetry. Oscillator strengths were calculated in the dipole length formalism by including only one-center contributions. The  $D$ -tensor was calculated from the sextet and quartet CI wavefunctions as discussed previously.<sup>42</sup> The spin–orbit coupling constants used were  $\zeta_{3d}(\text{Fe}) = 430 \text{ cm}^{-1}$ ,  $\zeta_{2p}(\text{N}) = 76 \text{ cm}^{-1}$ , and  $\zeta_{2p}(\text{O}) = 150 \text{ cm}^{-1}$ .

## Results and Analysis

**Abs, CD, and Low-Temperature MCD Spectroscopy.** The room-temperature Abs and CD and the low-temperature (LT) MCD spectra<sup>59</sup> of 3,4-PCD are shown in Figure 1 (solid lines). The Gaussian resolution (dashed line; obtained by simultaneous fitting of Abs, CD, and MCD, allowing for MCD bands to shift  $< 650 \text{ cm}^{-1}$  and sharpen at LT since LT Abs and CD spectra indicate no significant band shifts upon going to LT) of these spectra coupled with the VTVH MCD data (vide infra) indicated that seven bands (bands 1–7 in Figure 1) were required to fit the spectra over the region from 5000 to 35 000  $\text{cm}^{-1}$ . The experimental oscillator strengths ( $f_{\text{exp}}$ ) were calculated according to the approximation  $f_{\text{exp}} \approx (4.61 \times 10^{-9}) \epsilon_{\text{max}} \nu_{1/2}$ , where  $\epsilon_{\text{max}}$  is expressed in  $\text{M}^{-1} \text{ cm}^{-1}$  and the full width at half-maximum ( $\nu_{1/2}$ ) is expressed in  $\text{cm}^{-1}$ . The energies,  $\nu_{1/2}$ , Abs  $\epsilon$ , MCD  $\Delta\epsilon$ , and experimental oscillator strengths for ferric 3,4-PCD are given in Table 2. The oscillator strengths are too high for any of the bands to arise from d–d transitions which are all spin-forbidden in high spin  $d^5$  systems and therefore they are assigned as LMCT transitions.

**VTVH MCD Spectroscopy.** The simultaneous Gaussian resolution of the MCD, CD, and Abs data did not uniquely determine whether the large features at 31 150  $\text{cm}^{-1}$  and at 21 410  $\text{cm}^{-1}$  in the LT MCD spectra each consisted of one or two transitions. To resolve these regions, VTVH MCD data were collected at several points within these two bands. If the band was due to just one LMCT transition, the saturation behavior would be the same throughout the band, however, if the saturation behavior differs through the band envelope, there must be more than one transition present. The saturation behavior was different on either side of the peak maximum, and the saturation behavior at the maximum was a mixture of these for

(47) For the calculations the imidazole bond lengths were set to 2.14 Å from an earlier EXAFS refinement. Comparison of the ADF results of 2.14 Å to 2.10 Å showed no significant changes, so the 2.14 Å calculational results were used.

(48) te Velde, G.; Baerends, E. J. *J. Comput. Phys.* **1992**, *99*, 84–98.

(49) Baerends, E. J.; Ellis, D. E.; Ros, P. *Chem. Phys.* **1973**, *2*, 41–51.

(50) Vosko, S. H.; Wilk, L.; Nusair, M. *Can. J. Phys.* **1980**, *58*, 1200–1211.

(51) Becke, A. D. *Chem. Phys.* **1986**, *84*, 4524–4529.

(52) Perdew, J. P. *Phys. Rev. B* **1986**, *33*, 8822–8824.

(53) Frisch, M. J.; Trucks, G. W.; Schlegel, H. B.; Scuseria, G. E.; Robb, M. A.; Cheeseman, J. R.; Zakrzewski, V. G.; J. A. Montgomery, J.; Stratmann, R. E.; Burant, J. C.; Dapprich, S.; Millam, J. M.; Daniels, A. D.; Kudin, K. N.; Strain, M. C.; Farkas, O.; Tomasi, J.; Barone, V.; Cossi, M.; Cammi, R.; Mennucci, B.; Pomelli, C.; Adamo, C.; Clifford, S.; Ochterski, J.; Petersson, G. A.; Ayala, P. Y.; Cui, Q.; Morokuma, K.; Malick, D. K.; Rabuck, A. D.; Raghavachari, K.; Foresman, J. B.; Cioslowski, J.; Ortiz, J. V.; Baboul, A. G.; Stefanov, B. B.; Liu, G.; Liashenko, A.; Piskorz, P.; Komaromi, I.; Gomperts, R.; Martin, R. L.; Fox, D. J.; Keith, T.; Al-Laham, M. A.; Peng, C. Y.; Nanayakkara, A.; Gonzalez, C.; Challacombe, M.; Gill, P. M. W.; Johnson, B.; Chen, W.; Wong, M. W.; Andres, J. L.; Gonzalez, C.; Head-Gordon, M.; Replogle, E. S.; Pople, J. A. *Gaussian 98*; Gaussian, Inc.: Pittsburgh, PA, 1998.

(54) Due to the flat potential energy surface of these interactions IRC calculations converged to another stationary point which is quite similar ( $\Delta E < 0.2 \text{ kcal/mol}$ ) to the original one. Additional effort to eliminate these imaginary modes would not result in a significantly different molecular structure.

(55) Ridley, J.; Zerner, M. C. *Theor. Chim. Acta* **1973**, *32*, 111–135.

(56) Zerner, M. C.; Loew, G. H.; Kirchner, R. F.; Westerhoff, U. T. *J. Am. Chem. Soc.* **1980**, *102*, 589–599.

(57) Anderson, W. P.; Edwards, W. D.; Zerner, M. C. *Inorg. Chem.* **1986**, *25*, 2728–2732.

(58) Bacon, A. D.; Zerner, M. C. *Theor. Chim. Acta* **1979**, *53*, 21–54.

(59) A room-temperature MCD spectrum of this enzyme from *P. putida* has been reported in ref 31.

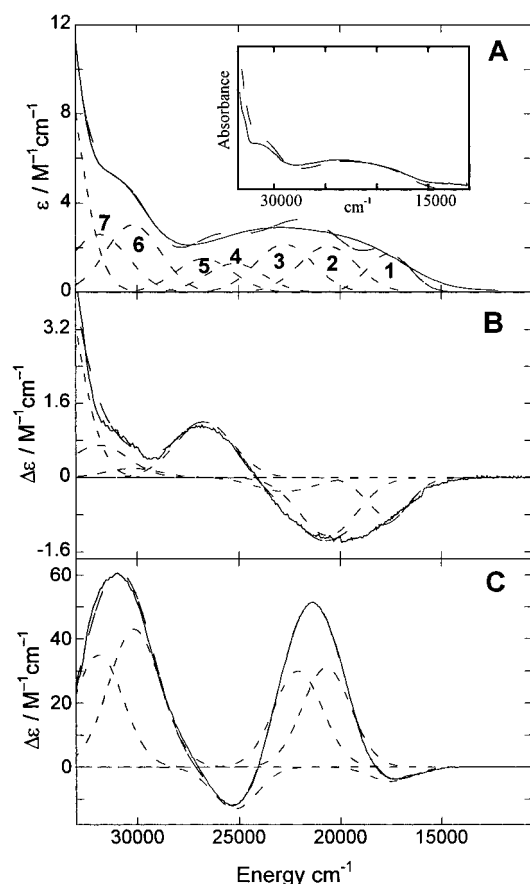


**Figure 1.** Gaussian resolution (---) of spectra (—) (A) Abs at 4 °C, (B) CD at 4 °C, and (C) MCD spectra at 5 K and 7 T. Inset shows overlay of low-temperature (—) and room-temperature (---) Abs. No features were observed between 5000 and 11 000  $\text{cm}^{-1}$ , and this region was omitted for clarity.

both the 21 410  $\text{cm}^{-1}$  and the 31 150  $\text{cm}^{-1}$  peaks (see Figure S1 in Supporting Information), indicating that there are two transitions contributing to each of these bands.<sup>60</sup> This requires that there are a total of at least seven LMCT transitions in the 5000–35 000  $\text{cm}^{-1}$  region.

In addition to clarifying the number of transitions, analysis of VTVH MCD data allows the polarizations of the transitions to be determined even for unoriented molecules in frozen solution. This information is important in assigning the transitions and in elucidating the electronic structure. VTVH MCD data were collected for six of the LMCT transitions (band 5 is not resolved in the MCD spectrum) at a variety of temperatures and fields for this Kramers system. The data were collected at or near the band maximum for the six Gaussian-resolved bands in such a way as to minimize contributions from overlapping bands (arrows in Figure 2A). The data were normalized and plotted as a function of  $\beta H/2k_B T$ . The variable-temperature MCD data and the saturation behavior of the six LMCT transitions (bands 1–4, 6–7) are shown as solid circles in Figure 2. The nesting observed for the different isotherms is expected for a Kramers system with ZFS, and the features are identified as MCD C-terms. A number of different nesting patterns are observed. The saturation magnetization behavior of bands 3 and

6 is very similar; they both quickly saturate and have more limited nesting. The saturation magnetization behavior of bands 2 and 4 is also similar; they are more nested than bands 3 and 6 and do not saturate at 7 T. Band 1 is very nested and passes through a maximum when  $\beta H/2k_B T = 0.35$ . Band 7 is also very nested but with a quite different shape, and it passes through a minimum when  $\beta H/2k_B T = 0.15$ .

VTVH MCD data can be fit (solid lines in Figure 2) using a theoretical approach based on the spin-Hamiltonian that relates the nonlinear MCD behavior to both transition polarization and spin-orbit coupling for systems with  $S \geq 1/2$  in low-symmetry molecular environments.<sup>38–40</sup> From experimentally determined spin-Hamiltonian parameters ( $D$ ,  $E/D$ ,  $g_x$ ,  $g_y$ , and  $g_z$ ), the effective transition moment products ( $M_{xy}^{\text{eff}}$ ,  $M_{xz}^{\text{eff}}$ , and  $M_{yz}^{\text{eff}}$ , where  $x$ ,  $y$ , and  $z$  refer to the principal axes of the  $D$ -tensor and  $M_{ij}^{\text{eff}} = m_i^{AK} m_j^{AJ} L_k^{KJ} \Delta_{KJ}^{-1}$ , where the transition from  $A$  to  $J$  is  $j$  polarized and transition from  $A$  to  $K$  is  $i$  polarized,  $L$  represents the perpendicular spin-orbit coupling component  $k$ , and  $\Delta$  is the energy separation of the excited state and single intermediate state)<sup>38,61</sup> can be determined from eq 1, where  $\gamma$  is a collection of constants,  $N_i$  is the Boltzmann population of the  $i$ th magnetic ground-state sublevel,  $\langle S \rangle_i$  is its spin expectation value in the direction indicated,  $l$  is a unit vector in the field direction, and  $\theta$  and  $\phi$  are the standard polar angles.<sup>62</sup>

$$\frac{\Delta\epsilon}{E} = \frac{\gamma}{4\pi S} \int_0^\pi \int_0^{2\pi} \sum_i N_i (l_z \langle S \rangle_i M_{xy}^{\text{eff}} + l_y \langle S \rangle_i M_{xz}^{\text{eff}} + l_x \langle S \rangle_i M_{yz}^{\text{eff}}) \sin \theta \, d\theta \, d\phi \, r \quad (1)$$

The percent polarization along the  $D$ -tensor axes can be estimated for each transition from the effective transition dipole products (eq 2) and cyclic permutations of the indices for the remaining two directions.<sup>38</sup>

$$\% x = 100 \left( \frac{(M_{xy}^{\text{eff}} M_{xz}^{\text{eff}})^2}{(M_{xy}^{\text{eff}} M_{xz}^{\text{eff}})^2 + (M_{xy}^{\text{eff}} M_{yz}^{\text{eff}})^2 + (M_{yz}^{\text{eff}} M_{xz}^{\text{eff}})^2} \right) \quad (2)$$

For high-spin ferric complexes, the principal  $g$ -values are isotropic. For 3,4-PCD (*B. fuscum*) the values of  $|D|$  and  $E/D$  had been previously determined by EPR (1.2, 0.33, respectively).<sup>44,63,64</sup> The sign of  $D$  (negative) will be determined later from INDO/S-CI calculations. The correct sign of  $D$  is important for determining polarizations since in the rhombic limit for an  $S = 5/2$  system with large ZFS, the effective  $g$ -values for the first and third Kramers doublets,  $g_{x,y,z}^{(1)}$  and  $g_{x,y,z}^{(3)}$ , are pairwise identical but with their order interchanged (Table 3).<sup>38,65</sup> Unlike EPR and magnetic susceptibility, where the results obtained for  $E/D = 0.33$  are independent of the sign of  $D$ , MCD selection rules give different saturation magnetization behavior for  $E/D = 0.33$  with a given polarization that depends on the sign

(61) Note that this definition is valid if a single intermediate state is responsible for most of the spin-orbit coupling intensity mechanism.

(62) Note that MCD measures the projection of the polarization components onto the direction defined by the principal axis system of the ZFS tensor. Therefore, the polarization and axis system do not need to be collinear. (See refs 38 and 66.)

(63) Que, L., Jr.; Lipscomb, J. D.; Zimmerman, R.; Münck, E.; Orme-Johnson, N. R.; Orme-Johnson, W. H. *Biochim. Biophys. Acta* **1976**, *452*, 320–334.

(64) Fujisawa, H.; Uyeda, M.; Kojima, Y.; Nozaki, M.; Hayaishi, O. *J. Biol. Chem.* **1972**, *247*, 4414–4421.

(65) Qualitatively this argument holds for the intermediate ZFS value of 1.2. Deviations will occur mainly at high fields, which is why an exact diagonalization is used.

(60) Having two transitions under the 21 500  $\text{cm}^{-1}$  MCD band was consistent with an earlier proposal based on resonance Raman<sup>35</sup> that there are Abs transitions at 22 222  $\text{cm}^{-1}$  for the equatorial tyrosinate and at 20 000  $\text{cm}^{-1}$  for the axial tyrosinate.

**Table 2.** Gaussian Resolution and Experimental Parameters for the Seven Observed Transitions of 3,4-PCD

band	Abs energy (cm <sup>-1</sup> )	$\epsilon$ (mM <sup>-1</sup> cm <sup>-1</sup> )	Abs $\nu_{1/2}$ (cm <sup>-1</sup> )	$f_{\text{exp}}^a$	MCD energy (cm <sup>-1</sup> )	$\Delta\epsilon$ (M <sup>-1</sup> cm <sup>-1</sup> )	MCD $\nu_{1/2}$ (cm <sup>-1</sup> )	polarization
1	17 600	1.7	3000	0.012	17 600	2.33	3000	y
2	20 600	2.0	4000	0.017	20 700	12.6	3400	z
3	22 750	2.0	4000	0.018	22 100	9.20	3400	y
4	25 200	1.1	4000	0.010	25 200	1.21	3000	z
5	26 700	1.3	3800	0.011				
6	30 200	3.0	4000	0.028	30 150	15.0	3600	y
7	31 850	2.6	3600	0.022	31 900	11.5	3400	z

<sup>a</sup> Where  $f_{\text{exp}}$  is the oscillator strength as described in the text.

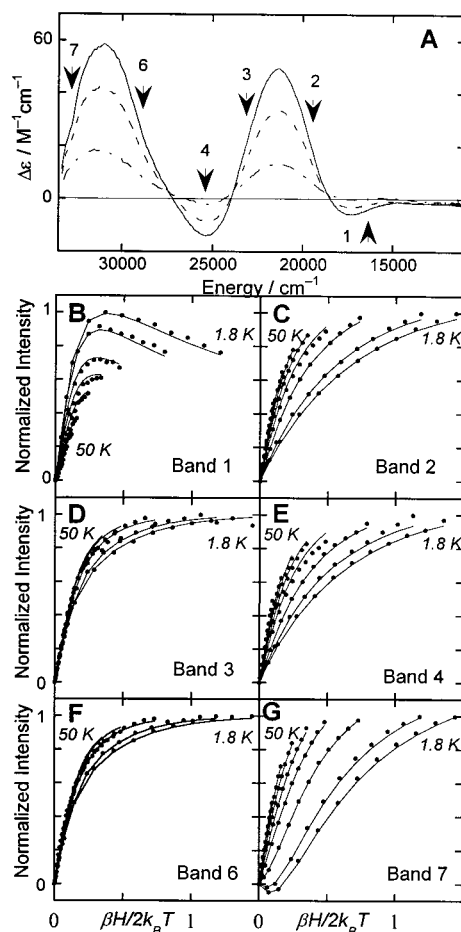


**Figure 2.** Variable-temperature-variable-field MCD data for 3,4-PCD. (A) Temperature dependence of the MCD spectrum at 7 T for 5 K (—), 15 K (---), and 50 K (· · ·); the arrows indicate where VTVH MCD data were taken. VTVH MCD data (•) collected between 0 and 7 T and between 1.6 and 50 K and the fit (—) at (B) 32 575 cm<sup>-1</sup> band 7, (C) 28 820 cm<sup>-1</sup> band 6, (D) 25 250 cm<sup>-1</sup> band 4, (E) 23 150 cm<sup>-1</sup> band 3, (F) 19 300 cm<sup>-1</sup> band 2, and (G) 16 390 cm<sup>-1</sup> band 1.

**Table 3.** Effective  $g$ -values for an  $S = 5/2$  System with  $E/D = 0.33$  and Large Negative ZFS

	$g_x$	$g_y$	$g_z$
$M_s = \pm 1/2$	0.86	9.69	0.61
$M_s = \pm 3/2$	4.29	4.29	4.29
$M_s = \pm 5/2$	0.86	0.61	9.69

of  $D$ .<sup>38–40</sup> Since the  $g$ -matrix and  $D$ -tensor are collinear (i.e., the true  $g$ -values are isotropic for  ${}^6A_1$ ),<sup>38</sup> a change in the order of the effective  $g$ -values for  $E/D = 0.33$  and  $D > 0$  versus  $D < 0$  leads to a corresponding interchange of two of the polarization directions.

Using the values for  $|D|$ ,  $E/D$  and  $g$  determined from EPR and the sign of  $D$  from INDO/S-CI calculations (vide infra),

the relative  $M_{xy}^{\text{eff}}$ ,  $M_{yz}^{\text{eff}}$ , and  $M_{xz}^{\text{eff}}$  values were obtained from eq 2 and used to calculate the percent  $x$ ,  $y$ , and  $z$  polarization of the transitions in which these directions are defined by the principal directions of the  $D$ -tensor. As shown in Table 2, the VTVH fitting reveals that band 1 is  $\sim 100\%$   $y$ -polarized, bands 2 and 4 are  $\sim 99\%$   $z$ -polarized, bands 3 and 6 are  $\sim 90\%$   $y$ -polarized and band 7 is  $\sim 73\%$   $z$ -polarized. Thus of the six LMCT transitions observed in MCD three (bands 1, 3, and 6) are  $y$ -polarized and three (bands 2, 4, and 7) are  $z$ -polarized, but none of the bands have any significant polarization in the  $x$ -direction. CT transitions are polarized along a given ligand–metal bond.<sup>66</sup> Previous resonance Raman data from 3,4-PCD showed that bands 2 and 3 are tyrosinate-to-iron CT transitions.<sup>35</sup> The polarizations obtained from the VTVH MCD data show that one tyrosinate is oriented along the  $z$ -axis and the other along the  $y$ -axis. From the INDO/S-CI calculations (vide infra), the directions of the  $D$ -tensor can be mapped onto the molecular coordinate frame, thus allowing the polarization information to be interpreted in terms of the specific tyrosinate–iron bonds.

**Molecular Orbital Calculations.** Both DFT and INDO/S-CI electronic structure calculations were performed in order to gain insight into the electronic structure of the active site of ferric 3,4-PCD and aid in the assignment of the seven experimentally observed LMCT transitions.

**A. Bonding Description.** The ground-state orbital energies and one-electron wavefunctions from the DFT calculations are summarized in Table 4. The four highest energy spin-down occupied molecular orbitals are on the tyrosinate ligands and involve the in-plane ( $6b_1$ ) and out-of-plane ( $3b_2$ ) O–Tyr lone pairs on each of the tyrosinates. These orbitals have a small amount of iron character ( $<13\%$  for each tyrosinate orbital). The five lowest unoccupied molecular orbitals have mainly Fe  $d$  character. The  $d_{z^2}$  orbital (these directions are relative to the calculated  $D$ -tensor coordinate system shown in Figure 3, vide infra) has the least amount of  $d$  character ( $\sim 66\%$ )<sup>67</sup> of the metal orbitals indicating that it is involved in a highly covalent interaction. The bonding interactions can also be seen in the contours of selected orbitals. The five unoccupied metal  $d$  orbitals obtained from the DFT calculations are shown in Figure 3, and the four highest energy occupied ligand orbitals are shown in Figure 4. The INDO/S-CI wavefunctions (Table S2 in the Supporting Information) had only slight differences: the amount of Fe  $d$  character in the ligand orbitals is lower ( $\sim 2\text{--}3\%$ ), there is a smaller contribution from the axial tyrosinate in the  $d_{yz}$  orbital, and there is a smaller contribution from the equatorial tyrosinate in the  $d_{xz}$  orbital.

(66) Zhang, Y.; Gebhard, M. S.; Solomon, E. I. *J. Am. Chem. Soc.* **1991**, *113*, 5162–5175.

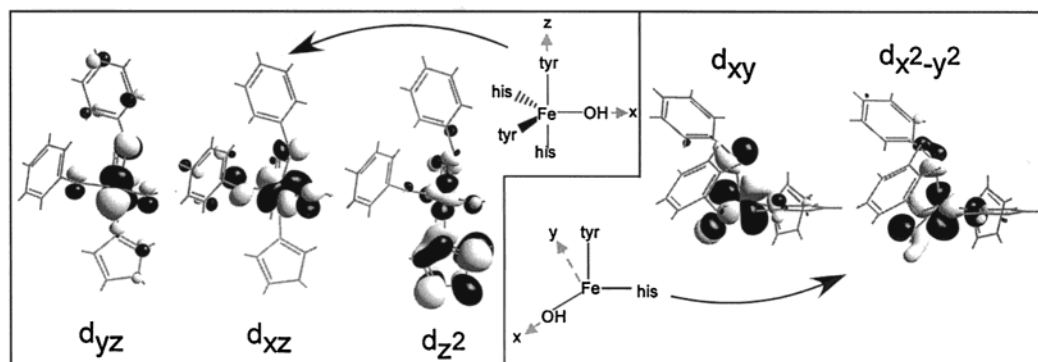
(67) The percentage was obtained by adding the sum of the  $d$  character in both orbitals 75 and 76 since they are close in energy and mixed.



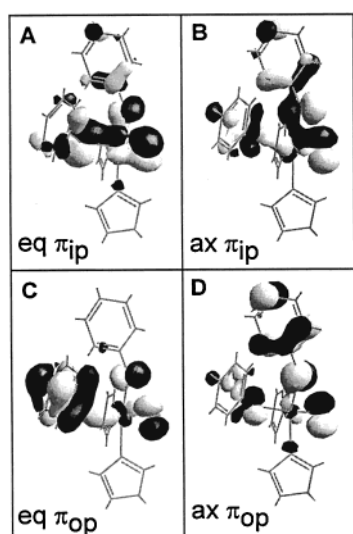
**Table 4.** MO Compositions Obtained for the Spin-Down Valence Orbitals in the Electronic Ground-State from the DFT Calculations<sup>a,b</sup>

level	label	energy (eV)	% d <sub>z</sub> <sup>2</sup>	% d <sub>x<sup>2</sup>-y<sup>2</sup></sub>	% d <sub>xz</sub>	% d <sub>xy</sub>	% d <sub>yz</sub>	% tyr ax ip	% tyr ax op	% tyr ax tot	% tyr eq ip	% tyr eq op	% tyr eq tot	% his ax	% his eq	% OH
76	z <sup>2</sup> + his π*	-1.498	44.9		1.7	1.6		2.1	1.1	3.2				24.0	10.2	5.1
75	z <sup>2</sup> + his π*	-1.605	15.1			1.3	1.4		1.1	1.1				6.8	7.0	1.4
74	x <sup>2</sup> - y <sup>2</sup>	-2.540	1.0	69.7	1.7	1.5					2.2	3.2	5.5		5.4	7.3
73	xz	-2.909	5.5		38.0	16.0	13.2	4.3		4.3	2.5	9.4	11.9		1.3	4.9
72	xy	-3.082		5.9	16.1	46.4	6.0				4.9	4.5	9.3		3.6	7.6
71	yz	-3.282		1.1	19.5		54.1	2.6	10.5	13.0	2.8		2.8	3.5		2.2
70	tyr ax op	-4.888					1.3	1.0	48.8	52.8	7.0	9.2	18.5	1.4		20.3
69	tyr eq op	-4.976				1.9	2.5	13.8		13.8		44.4	55.5			18.3
68	tyr ax ip	-5.337		1.1	1.2	8.5	2.2	19.7	17.7	41.0	4.0	9.8	18.9			19.8
67	tyr eq ip	-5.796			2.0	3.0	6.4	10.3	6.8	22.8	29.6		30.6	1.5		22.5

<sup>a</sup> The occupied orbitals are levels 67–70, and the unoccupied orbitals are levels 71–76. <sup>b</sup> Where ax = axial, eq = equatorial, op = out of plane, ip = in plane, his = histidine, tyr = tyrosine, and tot = total.

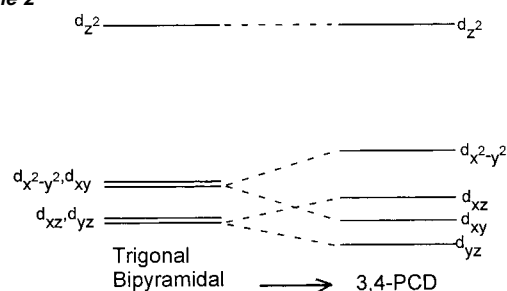


**Figure 3.** Molecular orbital contours of the five unoccupied spin-down metal MOs for 3,4-PCD from DFT calculations. See Table 4 for the orbital descriptions. The orbitals are from left to right MO 71, MO 73, MO 75, MO 72, and MO 74. For clarity, the three orbitals on the left are oriented as shown with the xz plane in the paper and the two orbitals on the right are oriented with the xy plane in the paper.



**Figure 4.** Molecular orbital contours of the four highest occupied spin-down tyrosinate MOs for 3,4-PCD from DFT calculations. These orbitals are oriented as indicated in the left of Figure 3. (A) MO 67. (B) MO 68. (C) MO 69. (D) MO 70.

The splitting pattern of the d orbitals of 3,4-PCD reproduced in Scheme 2 is consistent with a strong axial trigonal bipyramidal ligand field ( $d_{xz}, d_{yz}$ ) < ( $d_{xy}, d_{x^2-y^2}$ ) <  $d_{z^2}$  but with a large rhombic splitting of  $d_{xy}$  and  $d_{x^2-y^2}$ . The strong axial interaction involves the histidine and in particular the short axial phenolate–iron bond, and the rhombic splitting destabilizes the  $d_{x^2-y^2}$  orbital. The origin of this effect can be seen by comparing the contours of the  $d_{x^2-y^2}$  and  $d_{xy}$  orbitals (Figure 3). The  $d_{x^2-y^2}$  orbital is more directed along the equatorial metal–ligand bonds,

**Scheme 2**

in particular more  $\sigma$ -antibonding with the short phenolate–iron bond, which leads to the observed increase in energy of this orbital. The  $d_{xz}$  and  $d_{yz}$  orbitals are lowest in energy, but with  $d_{yz}$  slightly more stabilized than  $d_{xz}$ .

The MO calculations (Table 4) can be used to analyze the LMCT transitions observed for 3,4-PCD (Table 2). Of the three types of ligand (imidazolate, hydroxide, and phenolate), only the phenolate is expected to have LMCT transitions in the 5000–33 000  $\text{cm}^{-1}$  region. While imidazolyl ligands have potential  $\pi$ -donor interactions involving the out-of-plane  $\pi_1$  and  $\pi_2$  MOs,<sup>68</sup> these are limited since the coefficient in the MO of the nitrogen orbital that coordinates is small (especially for  $\pi_1$ ). Additionally, the  $\pi_1$  and  $\pi_2$  orbitals of the imidazolyl ligands are deeper in energy (the highest orbital is at -7.246 eV (from DFT), which is 11 600  $\text{cm}^{-1}$  lower in energy than the lowest tyrosinate valence orbital) and the expected transition energies from the INDO/S-CI and DFT calculations are significantly higher than the phenolate transitions. The hydroxide ligand has

(68) Guckert, J. A.; Lowery, M. D.; Solomon, E. I. *J. Am. Chem. Soc.* **1995**, *117*, 2817–2844.

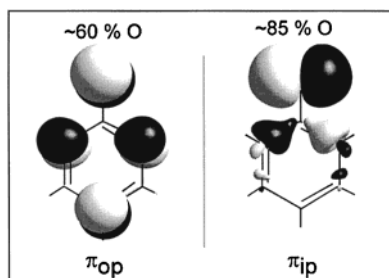


**Figure 5.** The  $\pi_{ip}$  and  $\pi_{op}$  molecular orbital contours of a free phenolate (where ip = in-plane and op = out-of-plane).

strong interactions with the metal site since the hydroxide character in the d orbitals is significant (Table 4, 2.2–7.6%). This is consistent with the observation that  $^{17}\text{O}$  hyperfine broadening is observed in the low-temperature EPR spectra of 3,4-PCD samples prepared with  $^{17}\text{O}$ -enriched water.<sup>33</sup> However, the energies of the CT transitions from the water-based ligand based upon the MO calculations (the highest hydroxide valence orbital is  $3600\text{ cm}^{-1}$  lower in energy than the lowest tyrosinate valence orbital) are higher than those of phenolate and thus at higher energy than the 280 nm protein cutoff. Therefore, just the phenolate LMCT transitions are in the energy region studied here as determined from the MO calculations and the previous observations of iron–phenolate transitions in the visible region for a wide variety of phenolate–Fe(III) systems (vide supra).

Free phenolate has three filled p orbitals on the oxygen atom. The oxygen 2p orbital that is oriented along the C–O bond is strongly involved in  $\sigma$  bonding to the carbon atom and therefore at much deeper binding energy. The remaining two oxygen 2p orbitals are contained in the  $\pi_{ip}$  and  $\pi_{op}$  molecular orbitals, where  $\pi_{ip}$  lies in the plane of the aromatic ring and  $\pi_{op}$  is perpendicular to the ring (Figure 5). The degree of conjugation into the ring differs for these two orbitals as seen by the greater amount of oxygen character in the  $\pi_{ip}$  orbital (80–85% by DFT) relative to the  $\pi_{op}$  (55–60% by DFT) orbital for the free phenolate. The lower percentage for  $\pi_{op}$  is due to significant orbital delocalization onto the C2, C4, and C6 atoms of the ring. The energies of the two valence orbitals for the free phenolate are split by  $5800\text{ cm}^{-1}$  with  $\pi_{ip} < \pi_{op}$ .<sup>69</sup> The phenolate–metal interaction depends on the Fe–O–C angle and the Fe–O–C–C dihedral angles, which are quite different for the two tyrosinates in all structurally defined 3,4-PCDs as discussed below. The net effect in the 3,4-PCD model is that the four highest occupied molecular orbitals are from the in-plane and out-of-plane lone pairs of the tyrosinate oxygen atoms from both the axial and equatorial tyrosinates. The in-plane orbitals are at lower energy than the out-of-plane orbitals, but the exact ordering within the in-plane and out-of-plane sets (i.e., axial vs equatorial) differs between the DFT and INDO/S calculations and can best be determined from experiment.

Based upon X-ray crystallography, the Fe–O–C angles are  $148^\circ$  and  $133^\circ$  for 3,4-PCD from *P. putida* and the Fe–O–C–C dihedral angles are  $24^\circ$  and  $68^\circ$  for the axial and equatorial tyrosinates, respectively (Table 1).<sup>14</sup> These bond angle differences lead the  $\pi_{ip}$  orbital of the axial tyrosinate to be directed more along the ligand–metal bond and the  $\pi_{op}$  orbital of the equatorial tyrosinate to be directed more along the ligand–metal

**Table 5.** Bond Order and Charge for DFT and INDO/S-CI Calculations

	charge			
	Mulliken (ADF)	Mulliken (INDO)	Hirschfeld (ADF)	Fe-frag overlap <sup>a</sup> (INDO)
tyr (ax)	−0.8	−0.7	−0.5	0.4
tyr (eq)	−0.5	−0.6	−0.4	0.5

<sup>a</sup> Fragment–fragment overlap, i.e., Fe with tyr (ax) and Fe with tyr (eq), the axial tyrosine and equatorial tyrosine, respectively.

bond. The MO calculations also indicate that the charges on the two tyrosinates are different as shown in Table 5. Together these results indicate that the axial tyrosinate, which retains more of its negative charge, has less interaction with the metal than the equatorial tyrosinate, which donates more charge to the iron. This can also be seen by examining the amount of metal character mixed into the occupied tyrosinate orbitals and the amount of tyrosinate character mixed into the d orbitals. For 3,4-PCD, there is 14% metal mixed into the axial tyrosinate and 16% into the equatorial tyrosinate, and 21% axial tyrosinate in the d orbitals and 30% equatorial tyrosinate in the d orbitals.<sup>70</sup> The greater degree of mixing for the equatorial tyrosinate, which is also seen in INDO/S-CI calculations (5.4% metal d in axial tyrosinate valence orbitals vs 6.9% metal d in the equatorial tyrosinate valence orbitals), indicates that the equatorial tyrosinate has a stronger bond with the metal. The  $\nu_{\text{CO}}$ 's obtained from Raman spectroscopy by Que and co-workers<sup>35</sup> also supports a weaker Fe–O bond for the axial tyrosinate. The  $\nu_{\text{CO}}$  for the axial tyrosinate ( $1266\text{ cm}^{-1}$ ) is at higher energy than the equatorial tyrosinate ( $1254\text{ cm}^{-1}$ ), indicating a stronger C–O bond, and therefore a weaker bond to the iron can be inferred. This trend has also been observed for methoxide bound to a metal ion surface site, which showed that as the C–O bond strengthened the M–O bond weakened.<sup>71</sup>

The impact of the geometry of the phenolate–metal bond angle upon bonding interactions was explored in a series of calculations where the axial phenolate Fe–O–C angle was varied from  $130^\circ$  to  $160^\circ$ .<sup>72,73</sup> The negative charge on the phenolate was found to increase consistently from  $-0.359$  to  $-0.374$  as the bond angle increased through the series. The energy of the  $d_{z^2}$  orbital (Figure 6) which is along the iron–phenolate bond decreased from  $-1.480$  to  $-1.646\text{ eV}$ . In contrast, the energy of the other four orbitals did not change significantly across the series with an average of  $-3.000 \pm 0.003\text{ eV}$ . Lastly, as the bond angle increased the percent axial tyrosinate character in the  $d_{z^2}$  orbital decreased from 12% to 7% across the series. Together these results indicate that the phenolate becomes less donating and has a weaker bonding interaction with the iron as the Fe–O–C angle increases.

To investigate whether the axial histidine ligand helps weaken the axial tyrosinate bond via a trans ligand influence, a model was calculated where the histidine–Fe(III) bond length was stepped from 2.1 to 2.3 Å. There was no significant change in

(69) This model was run with a point charge placed at the location of the iron in the 3,4-PCD structure.

(70) The metal character mixed into the tyrosinates was obtained by summing the d-orbital contributions to orbitals 68 and 70 for the axial tyrosinate and 67 and 69 for the equatorial tyrosinate. Similarly, the tyrosinate mixing into the d orbitals was obtained by summing the total axial and equatorial contribution to orbitals 71–76.

(71) Jones, P. M.; May, J. A.; Reitz, J. B.; Solomon, E. I. *J. Am. Chem. Soc.* **1998**, *120*, 1506–1516.

(72) The models for these calculations were based upon that used for the active site single point calculation with the additional simplification of replacement of the imidazoles with ammine ligands.

(73) Specifically,  $130^\circ$ ,  $135^\circ$ ,  $140^\circ$ ,  $147^\circ$ ,  $150^\circ$ , and  $160^\circ$  were calculated.



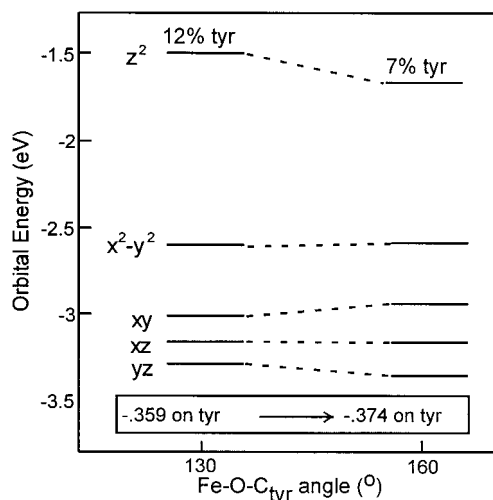


**Figure 6.** Trend in d-orbital energies and composition for the model as the Fe–O–C angle increases from 130° to 160°. The accompanying change in charge on the tyrosinate is shown in the box, and the changing tyrosinate composition of the  $z^2$  orbital is indicated.

bonding or charge of the axial tyrosinate, indicating that there is not a significant trans influence by this histidine.

**B. Orientation of the  $D$ -Tensor.** From the INDO/S-CI calculations, the  $D$ -tensor was mapped onto the coordinates of the 3,4-PCD active site by calculating the second-order spin–orbit coupling of the  $^6A_1$  ground state over the entire excited-state manifold of  $^4\Gamma$  and  $^6\Gamma$  states.<sup>38</sup> The  $D$ -tensor was calculated as described in ref 42, which upon diagonalization gives  $D_{xx} = 3.8795$ ,  $D_{yy} = 4.7365$ , and  $D_{zz} = 2.9737$  as the principal components where the spin-Hamiltonian parameters are defined as  $D = D_{zz} - (1/2)(D_{xx} + D_{yy})$  and  $E = (1/2)(D_{xx} - D_{yy})$ .<sup>74</sup> The  $z$ -direction was found to be oriented along the axial tyrosinate–iron bond, the  $x$ -direction was along the hydroxide–iron bond and the  $y$ -direction was oriented closest to the equatorial tyrosinate–iron bond (shown in Figure 3). These calculations yield an  $E/D$  of 0.32 and a  $D$  of  $-1.3 \text{ cm}^{-1}$  for 3,4-PCD. Fortunately, the magnitude of these values agrees remarkably well with the EPR-determined values of  $E/D = 0.33$  and  $|D| = 1.2 \text{ cm}^{-1}$ . Furthermore, these calculations provide the sign of  $D$  (negative) for 3,4-PCD, which is important since the MCD behavior differs for systems with  $-D$  as compared to  $+D$  even in the rhombic limit (vide supra). The orientation of the  $D$ -tensor relative to the molecular structure allows for the polarizations obtained from the VTVH MCD analysis to assign the tyrosinate  $\rightarrow \text{Fe(III)}$  CT transitions of 3,4-PCD.

**C. Spectral Assignments.** From the simultaneous Gaussian fitting of the CD, MCD, and Abs spectra there are seven LMCT transitions in the range of 5000–35 000  $\text{cm}^{-1}$ . By combining the information obtained from the variety of techniques discussed above, the seven LMCT transitions can now be assigned. Fitting of the VTVH MCD data for the six LMCT bands (band 5 is not observed in MCD) provided polarization information and showed that three of the bands were polarized along the  $y$ -direction and three were polarized along the  $z$ -direction. By mapping the  $D$ -tensor onto the active site, the VTVH MCD polarization directions can be related to the structure and the transitions can be assigned. The  $z$ -direction, which is the axial

**Table 6.** Calculated Excitation Energies and Oscillator Strengths for LMCT Transitions in DFT

energy <sup>a</sup> ( $\text{cm}^{-1}$ )	$f_{\text{osc}}^{a,c}$	energy <sup>b</sup> ( $\text{cm}^{-1}$ )	assignment
20 280	0.011	23 168	tyr ip eq to $yz$
21 894	0.012	ND <sup>d</sup>	tyr ip eq to $xy$
23 289	0.011	25 766	tyr ip eq to $xz$
26 266	0.006	28 235	tyr ip eq to $x^2 - y^2$
33 809	0.000	ND	tyr ip eq to $z^2$
16 578	0.015	20 243	tyr ip ax to $yz$
18 191	0.000	ND	tyr ip ax to $xy$
19 587	0.006	23 273	tyr ip ax to $xz$
22 563	0.000	26 324	tyr ip ax to $x^2 - y^2$
30 106	0.009	ND	tyr ip ax to $z^2$
13 666	0.000	21 555	tyr op eq to $yz$
15 279	0.012	ND	tyr op eq to $xy$
16 675	0.026	24 048	tyr op eq to $xz$
19 651	0.011	ND	tyr op eq to $x^2 - y^2$
27 194	0.000	ND	tyr op eq to $z^2$
12 956	0.025	ND	tyr op ax to $yz$
14 569	0.000	17 772	tyr op ax to $xy$
15 965	0.0002	ND	tyr op ax to $xz$
18 941	0.000	20 821	tyr op ax to $x^2 - y^2$
26 484	0.006	23 523	tyr op ax to $z^2/\text{his } \pi^*$
27 347	0.006	ND	tyr op ax to $z^2/\text{his } \pi^*$

<sup>a</sup> From ground-state calculation. <sup>b</sup> From promotion of 0.5 electron and reconverging. Using the method of Slater (*The Calculation of Molecular Orbitals*; John Wiley & Sons: New York, 1979), theoretical transition energies can be obtained from DFT calculations by transferring 0.5 electron between the ground and excited state and then calculating the difference between the energies of the one-electron orbitals involved in the transition. Also, oscillator strengths can be calculated from the ADF wavefunctions using the ligand–ligand overlap term of van der Avoird and Ros (*Theor. Chim. Acta* **1966**, *4*, 13–21). The oscillator strength can then be approximated as the sum of the overlap between the ligand-centered orbitals in the ground- and excited-state molecular orbitals. Metal-centered overlaps are ignored since they do not significantly contribute to  $f$ . This is depicted in eqs S1 and S2, where  $\Delta E$  is the transition energy and  $\vec{r}$  is the position vector to ligand  $a$ .  $C_{ab}$  and  $C_{ab}'$  are the coefficients of orbital  $b$  on ligand  $a$  for the ground- and excited-state molecular orbitals, respectively.

$$f_{\text{calc}} = (1.085 \times 10^{11})(\Delta E)|D|^2 \quad (\text{S1})$$

in which

$$D = \langle \Phi_L | \vec{r} | \Phi_L \rangle \sum_a \sum_b C'_{ab} C_{ab} \vec{r}_a \quad (\text{S2})$$

<sup>c</sup> In several of the transitions an artificially high  $f_{\text{osc}}$  was obtained due to ligand–ligand contributions from the hydroxide. Since the hydroxide to iron LMCTs are not in the energy region studied here, the  $f_{\text{osc}}$  values reported here contain only contributions from the two tyrosinates. <sup>d</sup> ND = not determined.

direction of the trigonal bipyramid, is approximately along the axial tyrosinate–Fe(III) bond, while the  $y$ -direction is pointed closest to the equatorial tyrosinate–Fe(III) bond. The CT transitions are expected to be polarized along the associated ligand–metal bond. Consequently, the three  $z$ -polarized transitions are from one of the axial ligands and the  $y$ -polarized transitions are from one or more of the equatorial ligands. The energy level diagram and the calculated transition energies also show that the energies of the histidine and hydroxide valence orbitals are much lower than the tyrosinate valence orbitals. Consequently, the energies of the associated LMCT transitions would be above the energy range accessible here (Table 6); therefore, all of the observed transitions must be due to the axial ( $z$ -polarization) or equatorial ( $y$  polarization) tyrosinates.

The experimentally calibrated energy diagram (shown in Figure 7) was derived from (1) the DFT order for the metal orbitals (a larger  $d_{xy}/d_{x^2-y^2}$  splitting than in INDO/S; for clarity only the DFT results are presented here, the INDO/S-CI results were similar), (2) the relative energy of the out-of-plane and

(74) Note that as discussed in ref 41, while the  $D$ -value may be negative the components must be positive because the sign of  $D_{ii}$  must be positive since  $\langle 0 | \text{H-SOC}(i) | I \rangle \langle I | \text{H-SOC}(i) | 0 \rangle$  is  $> 0$ .

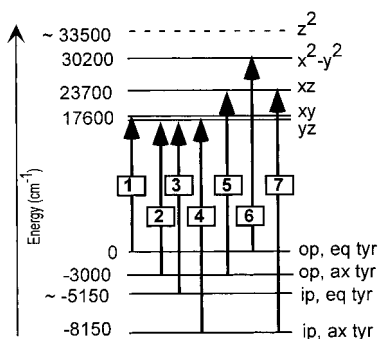


**Figure 7.** Experimentally calibrated energy level diagram with the assignment of observed transitions (bands 1–7) in 3,4-PCD.

the in-plane tyrosinate MOs ( $\pi_{op} > \pi_{ip}$ ), and (3) the polarizations of the observed transitions. The VTVH MCD data indicated that the lowest energy transition ( $17\,600\text{ cm}^{-1}$ ) was  $y$ -polarized and thus from the equatorial tyrosinate. Therefore, the order of the ligand orbitals within the  $\pi_{op}$  and  $\pi_{ip}$  sets was equatorial  $>$  axial. The splitting between the  $\pi_{ip}$  and  $\pi_{op}$  orbitals ( $\sim 5000\text{ cm}^{-1}$ ) in 3,4-PCD is large, which is consistent with that observed for the iron–tyrosinate protein uteroferrin ( $3000\text{ cm}^{-1}$ ).<sup>75</sup> The three  $y$ -polarized transitions are equatorial tyrosinate to metal CT transitions and are assigned as follows: band 1 is the  $\pi_{op}$  to  $d_{xy}$  transition, band 3 is the  $\pi_{ip}$  to  $d_{yz}$  transition, and band 6 is the  $\pi_{op}$  to  $d_{x^2-y^2}$  transition. These assignments are consistent with the orientation of the in-plane and out-of plane orbitals of the equatorial tyrosinate (Figure 4). The  $\pi_{op}$  orbital points toward the  $xy$  plane with a stronger  $\sigma$  interaction with the  $d_{x^2-y^2}$  orbital, leading to the higher intensity of band 6 relative to band 1. The  $\pi_{ip}$  orbital is approximately perpendicular to the  $xy$  plane and has interactions with the  $d_{yz}$  orbital. If there is a small amount of interaction with the  $d_{xz}$  orbital, it would be masked by band 6 and would not be observed here. The four  $z$ -polarized transitions are axial tyrosinate to metal charge-transfer transitions and are assigned as follows: band 2 is the  $\pi_{op}$  to  $d_{yz}$  transition, band 4 is the  $\pi_{ip}$  to  $d_{yz}$  transition, band 5 is the  $\pi_{op}$  to  $d_{xz}$  transition, and band 7 is the  $\pi_{ip}$  to  $d_{xz}$  transition. For the axial tyrosinate the orientation (Figure 4) is such that there are transitions from both the  $\pi_{op}$  and  $\pi_{ip}$  orbitals to the  $d_{xz}$  and  $d_{yz}$  orbitals. The main difference is that the  $\pi_{ip}$  orbital is pointed more toward the  $z$ -axis and therefore has more of a  $\sigma$ -type interaction. Also, a strong transition from the axial  $\pi_{ip}$  to the  $d_z^2$  orbital is anticipated from its orientation relative to the  $d_z^2$  orbital (Figures 3 and 4) and the significant mixing of the axial tyrosine into the  $d_z^2$  orbital (MOs 75 and 76 in Table 4). This transition should have the highest charge-transfer intensity since this transition involves mainly  $\sigma$  overlap. Although this transition is too high in energy to be observed since it is calculated at higher energy than the 280 nm protein cutoff, it can be predicted from the experimentally calibrated calculations to be almost as intense as the other axial transitions. Since the absorption spectrum for 3,4-PCD has a broad envelope of transitions, obtaining the exact distribution of oscillator strengths and hence assessing a difference in donor strength between the axial and equatorial tyrosinates is not possible from the absorption data.

Finally, the accuracy of the calculations can be evaluated from the experimentally calibrated energy level diagram. The  $d$  orbital

splitting pattern is reasonable for the distorted trigonal bipyramidal geometric structure. The predicted LMCT energies from DFT (Table 6) are consistently lower than the experimental values (Table 2), indicating that the calculation gives too covalent a description of bonding. The higher energies of the  $\pi_{op}$  orbitals relative to the  $\pi_{ip}$  orbitals are consistent with the different degree of bonding into the tyrosinate ring of the free ligand. The DFT calculations, however, show the axial tyrosinate orbital at higher energy than the equatorial tyrosinate orbitals. Also, the intensity ratio of transitions to the  $d_{yz}$  and  $d_{xz}$  orbitals does not correlate exactly with the experimental values. The experimental donor strength of the axial vs equatorial tyrosinates is higher than predicted from the calculation, but this is likely due to the difficulty in distributing the intensity to the four transitions under the broad absorption band. Despite these limited differences, the MO calculations do provide a reasonable description of the bonding in 3,4-PCD.

## Discussion

A combination of spectroscopic techniques has shown that 3,4-PCD has at least seven LMCT transitions in the region  $5000\text{--}35\,000\text{ cm}^{-1}$ . VTVH MCD was shown to be a powerful tool for resolving overlapping transitions. The six MCD-observed transitions from  $5000$  to  $35\,000\text{ cm}^{-1}$  are due to LMCT transitions from the equatorial or axial tyrosinate.

The VTVH MCD fits provided the main polarization directions of six of the LMCT transitions. When this information, which was previously only obtainable by single-crystal absorption spectroscopy, is correlated with the orientation of the  $D$ -tensor derived from electronic structure calculations, the transitions can be assigned to specific active site ligands. The assignments of the transitions were then obtained by correlating them with the energy-level diagrams, wavefunctions, and predicted transition dipole strengths obtained from quantum calculations. This showed that all seven LMCT transitions originate from charge transfer from the axial and equatorial tyrosinate lone pairs to the ferric center where transitions 2, 4, 5, and 7 (Figure 1) arise from the axial tyrosinate and transitions 1, 3, and 6 arise from the equatorial tyrosinate.

**Nature of the Phenolate–Iron Bond.** A high-spin ferric center in a spherical field has five degenerate  $d$  orbitals, all of which are half-occupied. The ligand field removes the degeneracy and these  $d$  orbitals split in energy. LMCT transitions are possible to any of these  $d$  orbitals<sup>76</sup> depending on the relative orientation of the ligand. For a tyrosinate ligand there are three  $p$  orbitals on the oxygen; however, the orbital pointed along the carbon in the ring is involved in the C–O bond and at much deeper binding energy, leaving only the two perpendicular  $\pi$ -type orbitals ( $\pi_{ip}$  and  $\pi_{op}$ ) for metal bonding. The presence of intense low-energy charge-transfer bands indicates that the tyrosinate ligand valence orbitals are close in energy to the iron  $d$  orbitals, and indicates high covalency in the tyrosinate–iron bonds.<sup>77</sup>

Both the Fe–O–C and the Fe–O–C–C angles influence the bonding interaction of the tyrosinate with the metal as shown

(75) Yang, Y.-S.; McCormick, J. M.; Solomon, E. I. *J. Am. Chem. Soc.* **1997**, *119*, 11832–11842.

(76) Or in the case of a spin-unrestricted calculation, as done here, to any of the five spin-down unoccupied  $d$  orbitals.

(77) This is due to the fact that the bonding interaction between the metal and ligand orbitals is proportional to  $H_{ML}^2/\Delta E$  ( $H_{ML}$  is the metal–ligand resonance integral, which increases as orbital overlap increases, and  $\Delta E$  is the energy difference between the metal and ligand orbitals), where a low transition energy would indicate a small  $\Delta E$  and a large bonding interaction.

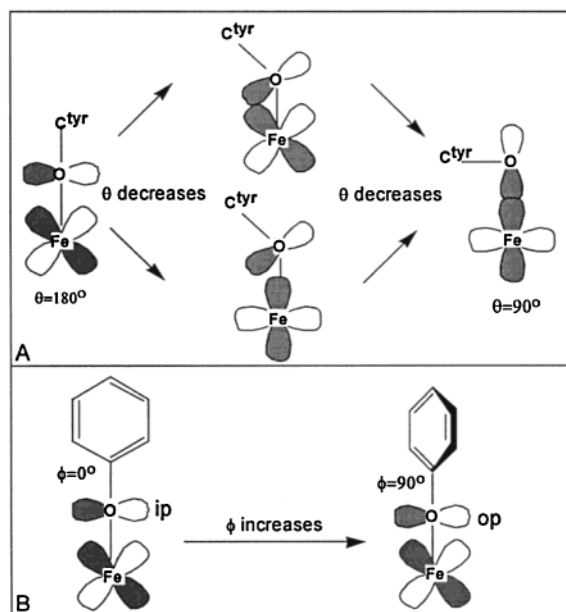


**Figure 8.** Schematic effects of bond angle alteration and molecular orbital overlap. (A) Effects of the Fe–O–C angle ( $\theta$ ) and (B) the Fe–O–C–C angle ( $\phi$ ) on orbital interactions.

schematically in Figure 8. At one extreme, the Fe–O–C angle is  $180^\circ$  and both the in-plane and out-of-plane orbitals on the tyrosinate have a  $\pi$  interaction with the metal center. As the Fe–O–C angle decreases, either the in-plane or out-of-plane orbital (depending on the dihedral angle) develops a pseudo- $\sigma$  interaction with the metal in addition to the  $\pi$  interaction. Considering the two limiting cases, if the dihedral angle is zero, then it is the in-plane orbital that develops the pseudo- $\sigma$  bonding, whereas if the dihedral angle is  $90^\circ$  then it is the out-of-plane orbital that develops the pseudo- $\sigma$  bonding. In the limit that the Fe–O–C angle is  $90^\circ$ , then the pseudo- $\sigma$  interaction becomes a pure  $\sigma$  interaction and there is no longer a  $\pi$  interaction (Figure 8A). If the dihedral angle is not  $0^\circ$ ,  $90^\circ$ , or  $180^\circ$ , then the situation becomes more complicated because now both the in-plane and out-of-plane orbitals can have strong pseudo- $\sigma$  interactions with the metal and the number of possible transitions increases to at least four (Figure 8B). Bending the Fe–O–C angle from  $180^\circ$  allows the two tyrosinate orbitals to maximize their interactions with the metal. Model complexes have shown that typical Fe–O–C angles for phenol and phenolic derivatives range from  $130^\circ$  to  $135^\circ$ , with the extreme examples as acute as  $110^\circ$  and as large as  $140^\circ$ .<sup>78</sup> Other iron–tyrosinate proteins such as transferrin and purple acid phosphatase have Fe–O–C angles of  $136^\circ$  and  $132^\circ$ , respectively.<sup>75,79–81</sup> It is interesting to note that while the trend of increased overlap at smaller angles is also observed for phenylthiolates,<sup>82</sup> the Fe–S–C angles for thiolates are consistently lower ( $100$ – $120^\circ$ ) than analogous Fe–O–C angles for alkoxides/phenolates. This is likely due to

the lower degree of 3s mixing into the 3p orbitals of the sulfur atom relative to the 2s mixing into the 2p orbitals of the oxygen atom.<sup>83</sup> Hence, the more p character in a particular orbital, the more acute the angle must be for strong  $\sigma$  overlap with the metal.

The metric parameters of the two tyrosinate–iron bonds in 3,4-PCD are different as shown in Table 1 and Scheme 1. Moreover, the difference in the orientation appears to play an important role in determining the energy of the associated transitions and the relative strength of the tyrosinate–Fe(III) bonds in 3,4-PCD. There are at least three transitions per tyrosinate in 3,4-PCD, and the axial tyrosinate has the dominant interaction with the  $\pi_{ip}$  orbital whereas the equatorial tyrosinate has the dominant interaction with the  $\pi_{op}$  orbital. The angle of the axial tyrosinate of 3,4-PCD from both *P. putida* and *A. calcoaceticus* ( $148^\circ$  and  $139^\circ$ , respectively) is significantly larger than the angle usually observed for phenolate–Fe(III) complexes. However, the bond lengths determined from EXAFS analysis for the two tyrosinates ( $1.88$  Å) are typical for phenols ( $1.75$ – $1.90$  Å).<sup>75,84</sup> Unfortunately, relevant high-spin phenolate–Fe(III) model complexes are rare in the October 2000 issue of the Cambridge Structural Database, and thus, meaningful correlations between bond angles and bond lengths (one of the indicators of bond strength) are not possible.

Our results from experimentally calibrated calculations show that while the equatorial tyrosinate  $\pi$  orbitals are higher than the axial orbitals the total charge donation including pseudo- $\sigma$  interactions is lower for the axial tyrosinate, demonstrating that the axial tyrosinate–iron bond is weaker than the equatorial tyrosinate–iron bond, even when the bond lengths are set equivalent as indicated by previous EXAFS analysis (Table 5). X-ray crystallography from *P. putida* indicated that the axial tyrosinate is  $0.09$  Å longer than the equatorial tyrosinate, although this difference is within the error of the structure. The resolution of the EXAFS data does not allow for detection of a  $0.09$  Å split in the two tyrosinates. However, if the axial tyrosinate–iron bond were indeed longer, this lengthening would only further weaken the axial tyrosinate–Fe(III) bond and enhance the electronic structure differences between the two tyrosinates.

The observed difference in bond strength between the two tyrosinates could be due to the electronic structure contributions from the other ligands in the trigonal bipyramidal site (i.e., axial vs equatorial) or to stereochemical constraints that weaken the axial tyrosinate or a combination of both. Geometry optimization of the first coordination sphere was used to investigate the role of the second coordination sphere interactions in helping to stabilize the axial tyrosinate in a weaker binding conformation and the equatorial tyrosinate in a strong binding conformation.<sup>53</sup> Two significant structural changes were observed (Table S3):<sup>85</sup> the ligands in the  $xy$  plane adopt angles closer to the usual trigonal value of  $120^\circ$  and perhaps most importantly the axial tyrosinate angle decreases from  $148^\circ$  to  $140^\circ$ . First, the changes upon minimization in the  $xy$  plane suggest that the approximately  $90^\circ$  angle (which is small for a trigonal bipyramidal geometry) between the equatorial tyrosinate and histidine ligands is

(78) Holm, R. H.; Kennepohl, P.; Solomon, E. I. *Chem. Rev.* **1996**, *96*, 2239–2314.

(79) Beck, J. L.; de Jersey, J.; Zerner, B. *J. Am. Chem. Soc.* **1988**, *110*, 3317–3318.

(80) Beck, J. L.; McConachie, L. A.; Summors, A. C.; Arnold, W. N.; de Jersey, J.; Zerner, B. *Biochim. Biophys. Acta* **1986**, *869*, 61–68.

(81) MacGillivray, R. T.; Moore, S. A.; Chen, J.; Anderson, B. F.; Baker, H.; Luo, Y.; Bewley, M.; Smith, C. A.; Murphy, M. E.; Wang, Y.; Mason, A. B.; Woodworth, R. C.; Brayer, G. D.; Baker, E. N. *Biochemistry* **1998**, *37*, 7919–7928.

(82) McNaughton, R. L.; Tipton, A. A.; Rubie, B. D.; Conry, R. R.; Kirk, M. L. *Inorg. Chem.* **2000**, *39*, 5697–5706.

(83) Kutzelnigg, W. *Angew. Chem., Int. Ed. Engl.* **1984**, *23*, 272–295.

(84) Carrano, C. J.; Carrano, M. W.; Sharma, K.; Backes, G.; Sanders-Loehr, J. *Inorg. Chem.* **1990**, *29*, 1865–1870.

(85) The equatorial tyrosinate rotated along the O–C bond ( $\sim 56^\circ$ ) such that its  $\pi_{ip}$  and  $\pi_{op}$  orbitals have nearly exchanged. This is driven by the formation of additional C–H $\cdots$ O hydrogen bonds which are not likely to be mechanistically important.



imposed by the protein second coordination sphere. This likely establishes an environment better suited to catalyze the dioxygenase reaction, rather than stabilize a more favorable metal binding site. Moreover, the distortion to the Fe(III) binding site is important since, upon substrate binding, the coordination geometry shifts to square pyramidal with an open position available to bind the distal end of a the substrate–peroxo intermediate. Thus, a tighter angle between the endogenous equatorial ligands provides a more accessible position in the substrate complex. This configuration, as well as additional active site features remote from the metal center, also establishes that the equatorial tyrosinate will be trans to the oxygen atom of the substrate that may subsequently ketonize (vide infra). Last, the 140° axial tyrosinate Fe–O–C angle in the minimized model is much closer to the typical iron–phenolate bond angles (vide infra). The smaller bond angle leads to more charge donation to the iron and consequently makes the bonding interaction more similar to that of the equatorial tyrosinate. Indeed, the Mulliken and Hirschfeld charges of each of the two tyrosinates are –0.4 in the minimized model. This contrasts sharply with the Fe(III) site in 3,4-PCD (Table 5) where both the Mulliken (–0.5 versus –0.8) and Hirschfeld (–0.4 versus –0.5) charges were higher for the axial tyrosinate. Together these results suggest that the characteristics that differentiate the two tyrosinate Fe(III) ligands and yield a distorted active site metal center must be largely due to the constraints of second coordination sphere interactions. Moreover, the higher energy associated with such a distorted coordination environment can effectively be dissipated by numerous interactions that propagate throughout the folded protein structure.

**Correlation with Reactivity.** The high intensity of the LMCT transitions indicates a high degree of covalency in the two tyrosinate–Fe(III) bonds, which would lower the reduction potential and stabilize the oxidized iron site. In contrast, extradiol dioxygenases such as catechol 2,3-dioxygenase contain an active site ferrous center that is stable in the ferrous state even when exposed to oxygen for long periods of time.<sup>86</sup> Crystal structures have shown that the extradiol dioxygenases utilize a 2-His, 1-Glu facial triad<sup>2</sup> to stabilize the ferrous metal center.<sup>87–89</sup> Thus, the iron ligation in the intra- and extradiol dioxygenases is similar in that they are both five-coordinate and have two histidines. They differ in that the intradiol dioxygenases have the two tyrosines and a hydroxide while the extradiol dioxygenases have a glutamate and two water ligands. Upon substrate binding both experience significant perturbation to the iron coordination sphere and adopt a square pyramidal geometry quite different from the resting structure.<sup>12,90</sup> In each case the substrate binds to the iron as an asymmetric chelate, but it displaces the axial tyrosine and the solvent in the intradiol dioxygenases and the two water ligands in the extradiol dioxygenases. The presence of tyrosinate ligands helps maintain the intradiol dioxygenase site in the oxidized state. Since all previous experimental results on 3,4-PCD have failed to indicate the presence of an Fe(II)–semiquinone state in the anaerobic substrate complex, it is

proposed that O<sub>2</sub> attacks an activated form (perhaps ketonized) of the substrate ring. This is in clear contrast to the ferrous site of the extradiol enzymes that increase the affinity for NO, and presumably O<sub>2</sub> binding in the substrate-bound complex.

The mechanistic role of the axial tyrosinate in the binding of substrate is supported by the Y447H mutant studies where slow substrate binding and product release contributed to a 600-fold decrease in  $k_{\text{cat}}$ .<sup>11</sup> The geometric and electronic structure of the WT active site indicate that the axial tyrosinate–iron bond is weakened by its geometry and thus it can dissociate more readily upon substrate binding. Thus, it may serve as an active site base to remove the second proton from the substrate molecule and also potentially aid in modulation of the redox potential of the site (Scheme 1). The equatorial tyrosinate has a stronger bond and a smaller Fe–O–C angle that remains upon binding of substrate, which is consistent with its proposed role in lengthening of the substrate bond trans to it.<sup>12–14</sup> Additionally, only the axial tyrosinate was shown to have any significant solvent exposed surface and may more easily reorient upon substrate binding.<sup>35</sup> Thus the two tyrosinates act in a concerted fashion to facilitate the activation of PCA, perhaps via a ketonization process and modulation of the redox potential of the site. The open binding site in the anaerobic substrate complex is adjacent to the putative O<sub>2</sub> binding cavity, which is created by the PCA ring, the equatorial tyrosinate, and the new orientation of Tyr447. The juxtaposition of the cavity to the site of reaction is consistent with mechanistic proposals that call for the direct electrophilic attack by dioxygen at the C4 carbon of the PCA ring, which may result from an increase in anion or radical character at this position. The active site geometric and electronic structure of 3,4-PCD and other members of the family, therefore, appears to be fine-tuned to bind aromatic substrates, activate the chelated complex by an as-yet unknown process, and then direct the subsequent dioxygen attack at the correct site to yield intradiol ring cleavage. Our results demonstrate that some of the most critical features responsible for this fine-tuning process are related to the orientation of the two tyrosinate ligands in the Fe(III) coordination sphere.

In summary, spectroscopic analyses combined with theoretical calculations have provided a detailed description of the electronic structure of the ferric active site of 3,4-PCD. The spectral features of 3,4-PCD are attributed to the in-plane and out-of-plane lone pairs of the axial and equatorial tyrosinates. Analysis of the CT bands shows that the tyrosinate–Fe(III) bond is determined in large part by the extent of pseudo- $\sigma$  interaction which increases with decreasing Fe–O–C angle. The energy of the transitions as well as the bond order and overlap of the two tyrosinate ligands indicates that the axial tyrosinate is more weakly bound to the ferric center than the equatorial tyrosinate. Combined with the higher solvent accessibility of the axial tyrosinate, this indicates that the axial tyrosinate can more easily dissociate upon substrate binding. The strong equatorial tyrosinate–Fe(III) bond may promote the ketonization of the substrate via a trans influence. Thus, this study has shown that the active site of 3,4-PCD evolved to use the same residue, tyrosinate, in two essential but very different roles by controlling the coordination geometry of the tyrosinate–Fe(III) bonds.

**Acknowledgment.** We thank Dr. Robert Szilagyi for assistance with the Gaussian 98 calculations. This research was supported by NIH Grant GM40392 (E.I.S.) and NIH Grant

(86) Hori, K.; Hashimoto, T.; Nozaki, M. *J. Biochem.* **1973**, *74*, 375–384.

(87) Kita, A.; Kita, S.; Fujisawa, I.; Inaka, K.; Ishida, T.; Horiike, K.; Nozaki, M.; Miki, K. *Structure* **1998**, *7*, 25–34.

(88) Sugimoto, K.; Senda, T.; Aoshima, H.; Masai, E.; Fukuda, M.; Mitsui, Y. *Struct. Fold. Des.* **1999**, *7*, 953–965.

(89) Han, S.; Eltis, L. D.; Timmis, K. N.; Muchmore, S. W.; Bolin, J. T. *Science* **1995**, *270*, 976–980.

(90) Bolin, J. T. Personal communication.

GM24689 (J.D.L.). M.I.D. thanks the Evelyn Laing McBain Fund for a doctoral fellowship. F.N. thanks the Deutsche Forschungsgemeinschaft for a postdoctoral fellowship. J.M.Z. thanks the Jane Coffin Childs Fund for Medical Research for a postdoctoral fellowship. The computing facilities of the Department of Chemistry at Stanford University are supported in part by a grant from the National Science Foundation (CHE-9408185).

**Supporting Information Available:** Saturation data for 31 150  $\text{cm}^{-1}$  and 21 410  $\text{cm}^{-1}$ , Cartesian coordinates used for DFT and INDO/S-CI calculations, MO compositions and energies from INDO/S-CI, and geometry-optimized coordinates from Gaussian 98 (PDF). This material is available free of charge via the Internet at <http://pubs.acs.org>.

JA011945Z